

Manuscript version: Author's Accepted Manuscript

The version presented in WRAP is the author's accepted manuscript and may differ from the published version or Version of Record.

Persistent WRAP URL:

<http://wrap.warwick.ac.uk/160238>

How to cite:

Please refer to published version for the most recent bibliographic citation information.

Copyright and reuse:

The Warwick Research Archive Portal (WRAP) makes this work by researchers of the University of Warwick available open access under the following conditions.

Copyright © and all moral rights to the version of the paper presented here belong to the individual author(s) and/or other copyright owners. To the extent reasonable and practicable the material made available in WRAP has been checked for eligibility before being made available.

Copies of full items can be used for personal research or study, educational, or not-for-profit purposes without prior permission or charge. Provided that the authors, title and full bibliographic details are credited, a hyperlink and/or URL is given for the original metadata page and the content is not changed in any way.

Publisher's statement:

Please refer to the repository item page, publisher's statement section, for further information.

For more information, please contact the WRAP Team at: wrap@warwick.ac.uk.

Enhanced stability of tin halide perovskite photovoltaics using a bathocuproine - copper top electrode

Anjana Wijesekara¹, Marc Walker², Yisong Han², David Walker², Steven Huband² and Ross Hatton^{1}*

¹Department of Chemistry, University of Warwick, CV4 7AL, Coventry, United Kingdom.

²Department of Physics, University of Warwick, CV4 7AL, Coventry, United Kingdom.

*Corresponding Author. E-mail: Ross.Hatton@warwick.ac.uk

Keywords: perovskite solar cell, perovskite photovoltaic, tin perovskite, copper electrode, bathocuproine

Abstract

Unencapsulated organo-tin halide perovskite photovoltaic (PV) devices exhibiting record stability (for organo-tin perovskite PV devices) when tested under continuous one sun solar illumination in ambient air and under electrical load are reported. This exceptional stability is made possible by the use of a bathocuproine | copper cathode in an inverted device architecture. A series of experiments designed to elucidate the underlying reasons for the high stability show that, compared to conventional silver electrodes, compact copper electrodes are far more resistant to corrosion by I₂ gas (evolved when organo-tin halide decomposes) and toward adverse morphological evolution and ingress of oxygen and water molecules through the top electrode into the device. The findings of these experiments show that copper should be the metal of choice for the reflective cathode in inverted tin perovskite PVs when the material interfacing the metal interacts strongly with it, enabling compact film formation and a stable interface towards copper diffusion into the adjacent charge transport layer.

1. Introduction

In recent years there has been rapidly growing interest in research into tin halide perovskites as the light harvesting semiconductor in photovoltaic (PV) devices.^[1,2] Tin perovskites have the advantage over their lead analogues that they do not contain lead, which is a toxic element well known to bio-accumulate.^[3] Lead halide perovskites decompose upon exposure to the ambient environment forming water soluble lead containing compounds, and so their use in PVs inevitably presents an environmental and toxicological risk, not only if device encapsulation fails in the field, but also at the end of their useful life.^[3] The latter requires that the devices are very carefully disposed of, which is difficult to guarantee for products with a useful lifetime of decades. Tin perovskites also offer narrower bandgaps than their lead analogues, enabling a greater proportion of the solar spectrum to be harvested.^[4] The Achilles' heel of tin perovskites for PV applications is their higher susceptibility to oxidation in air which stems from the tendency of Sn^{2+} to convert to the more thermodynamically stable +4 oxidation state upon exposure to ambient air.^[5] The intrinsic resistance of the device stack to air ingress dictates the degree of packaging required for practical applications, and thus the packaging cost, so there is a need to identify ways to make tin perovskite PVs more intrinsically stable.^[1,2] Strategies to achieving this goal include making the perovskite more stable by compositional engineering or defect passivation^[6] and/or making the other parts of the device stack capable of blocking water and oxygen ingress, without compromising their electronic function^[7] (e.g. by introducing hydrophobic charge transporting layers).^[8,9]

To date thermally evaporated gold (Au), silver (Ag) or aluminium (Al) films with a thickness of ≥ 100 nm are most widely used as the reflective electrode in tin perovskite PVs due to the high reflectivity of these metals across the visible and near-infra red spectrum together with their low electrical resistivity. Whilst Au is viable in the research environment it is too expensive for practical application on a large scale (the price of Au in 2021 is more than 68

times that of Ag^[10]) and Au is also known to diffuse into the device undermining the integrity of the diode.^[11] Ag is a more economically viable alternative to Au, although several studies of lead perovskite PVs have shown that the Ag electrode is a source of device instability because it is corroded by the iodine containing degradation products of lead perovskite, reverting to the transparent insulator AgI.^[12-14] Unfortunately, substitution of Ag with Al is also not a viable option, since Al electrodes interfacing the organic semiconductors used to transport electrons in perovskite PVs have proved to be unstable.^[15]

Copper (Cu) is attractive as an alternative to Ag because the cost of Cu is ~100 times lower than Ag, with a comparable electrical conductivity. Whilst the reflectance of Cu at wavelengths less than 600 nm is < 50% that of Ag, due to the 3d to 4s electronic transitions, this corresponds to the region over which tin halide perovskites absorb most strongly, so for the perovskite thickness typically used in PV devices of several 100 nanometres all of the short wavelength light can be absorbed upon first pass through the perovskite.^[16,17] Promisingly, reaction of Cu with lead halide perovskite in the absence of oxygen and water has also been shown to be much slower than Ag and Al.^[18] However, in perovskite PV devices that can achieve high power conversion efficiency the cathode is invariably separated from the perovskite layer by a charge carrier selective interfacial layer (e.g. C₆₀ or phenyl-C₆₀-butyric acid methyl ester (PCBM)) and so the perovskite is not in direct contact with the cathode. Of greater relevance is the intrinsic stability of the electrode toward the decomposition products of the perovskite, since air ingress results in degradation of the perovskite forming corrosive small molecules such as I₂, PbI₂ and HI that easily diffuse through the charge transport layer(s) and corrode the metal electrode.^[19] The iodine containing decomposition products of organo-lead halide perovskites have been shown to react with Cu to form CuI, which erodes the electrode conductance and impedes the process of charge carrier extraction.^[20]

The disadvantage of Cu as an electrode metal is its higher susceptibility to oxidation in air than either Ag or Au.^[20,21] However, our group and others have shown that the rate of oxidation of Cu films actually depends strongly on the structure and morphology of the film and can be extremely slow after oxidation of the first few nanometres, even for polycrystalline Cu films.^[22–24] This implies that for the metal thickness used as an opaque electrode of ≥ 100 nm, oxidation of the top exposed surface of the Cu electrode is unlikely to be the fastest degradation mechanism in a perovskite PV device. Indeed, a Cu top electrode could actually serve the dual role of low cost cathode and built-in desiccant for low levels of oxygen and water ingress in encapsulated PV devices.

Despite the aforementioned advantages there are very few reports pertain to use of Cu as the top contact in perovskite PVs.^[18,20,21,25–29] Those that do show that the initial performance is comparable to that using a Ag electrode^[21] and that the device shelf-life can exceed that of identical devices using a Ag electrode^[18], although initial device performance is rarely a good indicator of stabilised device performance under continuous illumination and load. Similarly a long shelf-life does not necessarily translate to high operational stability, since some degradation mechanism of metal halide perovskites are light and heat and electric field induced and/or accelerated.^[7] Promisingly, Li *et al.* have shown that CsSnI₃ perovskite inverted PV devices maintained $>90\%$ of their starting efficiency after 500 hrs light soaking when encapsulated with glass.^[30] To understand the intrinsic stability of perovskite PVs with a Cu top electrode towards degradation in ambient air, which inevitably ingresses into the device even with encapsulation, it is useful to test the devices in ambient air under 1 sun constant illumination and under electrical load. Without device encapsulation such a test is clearly an accelerated degradation test, since for practical application PV devices would always be encapsulated and so the rate of air ingress into the device would be many orders of magnitude slower. However, such accelerated tests are useful because they help researchers to quickly

identify promising materials and device designs for long-life applications such as PVs. Without device encapsulation wholly inorganic tin perovskites have proved to be the most stable type of tin perovskite PV when tested in ambient air; Table S1^[28, 31-37], although it is notable that none of the reports relate to device testing under load. Similar to the case of lead perovskites, the power conversion efficiency of inorganic tin perovskites lags far behind that of organo-tin halide perovskites and so there is a need to find ways to stabilise organo-tin halide perovskites for PV applications.¹ Promisingly, Wang *et al.*^[31] have shown that PV devices based on $\text{HC}(\text{NH}_2)_2\text{SnI}_3$ perovskite with SnCl_2 and gallic acid additives retained 80% of their starting efficiency after 1000 hours storage in ambient air. However, when tested without encapsulation in air the power conversion efficiency (η) decreased by 30% within 2.3 hours.

To the best of our knowledge, to date there is only one publication that reports the stability of perovskite PV devices under constant 1 sun illumination in air under electrical load using a Cu electrode, and it pertains to lead perovskite rather than tin perovskite.^[21] The chemistry of tin perovskite degradation in air is not the same as that of the analogous lead perovskite because, unlike tin, lead is most stable in the 2+ oxidation state. Consequently, it cannot be assumed that modes of degradation in a tin perovskite PV are the same as that reported for lead perovskite PVs. Lin *et al.*^[21] have reported enhanced stability in inverted lead perovskite PVs by inserting a 10 nm Cu layer between the bathocuproine (BCP) electron extraction layer and 100 nm Ag cathode, as compared with devices using the single metal electrodes Al, Ag or Cu. Based on analysis of degraded devices using depth profiling secondary ion mass spectrometry those authors concluded that insertion of a 10 nm Cu layer at the interface between the 100 nm Ag electrode and BCP electron extraction layer reduces diffusion of corrosive iodine containing species originating from the decomposing perovskite through the 60 nm thick PCBM electron transport layer and 6 nm thick BCP layer, whereupon they corrode the metal cathode. Given that the 10 nm Cu layer was separated from the lead perovskite layer

by 66 nm of organic semiconductor (6 nm BCP plus 60 nm PCBM), it is not clear as to how the 10 nm Cu layer could impede diffusion from the perovskite into the PCBM layer. Using a 100 nm thick Ag electrode together with a 10 nm Cu layer also means that there is no material cost advantage over using a 100 nm Ag electrode.

Herein we report exceptional stability for an unencapsulated organo-tin halide perovskite PV device when subject to continuous 1 sun solar illumination in ambient air and under electrical load, when using a BCP | Cu (100 nm) cathode. We also elucidate the underlying physical reasons for the stabilising effect of the BCP | Cu cathode as compared to the conventional BCP | Ag cathode.

Results and discussion

For the purpose of this study tin halide perovskite $\text{FA}_{0.78}\text{GA}_{0.2}\text{SnI}_3\text{-1\% EDAI}_2$ with 10 mol% SnF_2 was synthesised according to an adaptation of the method of Jokar *et al.*^[38], where EDA_2I_2 is ethylenediammonium diiodide, and FA and GA are A-site formamidinium and guanidinium cations respectively. This organo-tin perovskite was chosen because at the start of this study it had been reported to exhibit the highest power conversion efficiency for a tin perovskite PV device (Average PCE; 7.4 % \pm 0.3 and champion PCE; 8.5%). PV devices with the inverted structure; ITO| poly(3,4-ethylenedioxythiophene) polystyrene sulfonate (PEDOT:PSS) (Al 4083)| $\text{FA}_{0.78}\text{GA}_{0.2}\text{SnI}_3\text{-1\% EDAI}_2$ +10 mol % SnF_2 (110 nm) | C_{60} (32.5 nm)|cathode were fabricated in a nitrogen filled glovebox (\leq 1 ppm O_2 and H_2O). The cathodes studied were BCP (6 nm) | Ag (100), BCP (6 nm) | Cu (100) and Cu (100 nm). All devices were tested under continuous 1 sun simulated illumination using a class AAA Xenon-arc lamp solar simulator with devices under load operating close to the maximum-power-point using a fixed voltage bias. The temperature of the devices stabilised at 43 °C. The relative humidity fluctuated in the range 30%-50%. The average (and champion) power conversion efficiency measured for 30 devices

of each type in a nitrogen filled glovebox before stability testing was 5.4 (6.4)%, 5.2 (6.2) % and 5.8 (6.9) % for devices with BCP|Ag, Cu and BCP|Cu cathodes respectively.

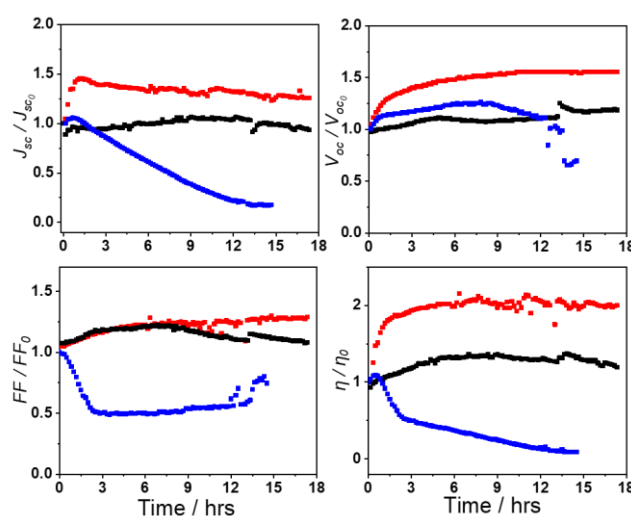


Figure 1 | Representative relative change in J_{sc} , V_{oc} , FF and η for unencapsulated PV devices with the structure ITO|PEDOT:PSS (Al 4083)|perovskite|C₆₀|cathode tested in ambient air under continuous 1 sun simulated solar illumination with the device under load. Cathode: (red) BCP |Cu; (black) Cu without BCP; (blue) BCP | Ag.

The data in **Figure 1** and the evolution of the absolute device parameters given in S1-S3, show that when unencapsulated PV devices are tested under load in ambient air, those using a BCP|Ag electrode degrade quickly and those using a BCP|Cu cathode are remarkably stable for PVs based on an organo-tin perovskite light harvesting layer: Over 17.3 hours the power conversion efficiency (η) of devices with a BCP|Cu cathode decreases between 0-14%, with 50% of the devices exhibiting no deterioration at all (Figure S1-2). For the champion device the power conversion efficiency degraded to 70% of its peak value (which was achieved within 100 min) only after 44.5 hrs: Figure S4. To our knowledge this is the highest stability reported for an unencapsulated organo-tin halide perovskite PV device by a considerable margin: The rate of deterioration in power conversion efficiency is less than half the previously reported best stability for an organo-tin perovskite based PV tested in ambient air (Table S1). Conversely,

the power conversion efficiency of devices using a conventional Ag electrode decreased by $\geq 80\%$ from their peak efficiency within 14 hours. When tested over the same time period in a nitrogen filled glovebox devices using a BCP|Ag and BCP|Cu electrode exhibited no degradation (Figure S5), consistent with the report of Jokar *et al.* who showed that devices using the same perovskite and architecture with a BCP|Ag cathode are stable in a nitrogen atmosphere.^[38] The degradation in performance upon testing in ambient air can therefore be attributed to degradation resulting from ingress of oxygen and/or water into the device. Whilst in the context of the current study the rate of device degradation after the maximum performance has been achieved is of most relevance, it is notable that the performance of devices using both Ag and Cu electrodes initially improves before the onset of degradation (Figure 1 and S1-S4), such that the champion power conversion efficiencies for devices with BCP|Ag, Cu and BCP|Cu cathodes increases to 6.4%, 7.4% and 10.1% respectively. Whilst it is not unusual for there to be burn-in processes in perovskite PVs, such processes are normally associated with deterioration in device performance rather than an improvement.^[39] Notable exceptions to this are two previous reports from our group that inverted tin perovskite PVs exhibit an improvement in power conversion efficiency upon light soaking, which is shown to result from the gradual diffusion of excess tin halide (in those cases SnI₂ and SnCl₂) into the fullerene electron-transport layer where it serves as an *n*-type dopant suppressing current leakage across the device and recombination losses at the site of pinholes in the perovskite film where the fullerene layer contacts the hole-extracting electrode.^[32,37] It is likely that a similar process is occurring here, since the device architecture is the same and there is excess tin halide in the perovskite film (in this case SnF₂). In the early stages of device testing this efficiency enhancing process initially dominates over the processes giving rise to device degradation, so peak device efficiency is not achieved until after the start of the constant illumination test. Since for devices using a Cu electrode the rate of device degradation is much slower (the reason for which is elucidated in this paper) the peak in efficiency occurs later than for devices using a Ag

cathode. Interestingly, the improvement in performance is made even more pronounced because the starting efficiency for devices tested under load is consistently lower than devices which are held in the open-circuit condition immediately prior to device testing, the reason for which is the subject of investigation.

In order to understand why devices using a Cu cathode are so much more stable than those using a conventional Ag electrode it is useful to first understand why those using a Ag cathode degrade so quickly in ambient air. There have been a number of studies reporting how Ag electrodes can be a source of instability in lead perovskite PVs^[12,40], although to our knowledge none pertaining to tin perovskite PVs. Given that the chemistry of tin perovskite degradation in air is not the same as for the lead analogue it cannot be assumed that the mechanism of cathode degradation in tin perovskite PVs is the same as that previously reported for lead perovskite PVs. It is evident from Figure S3 that, whilst there is a large spread in the rate of degradation in open-circuit voltage (V_{oc}) and fill-factor (FF) across different devices, all devices with a Ag cathode exhibit a continuous rapid decline in short-circuit current density (J_{sc}), after an initial small increase within the first hour, such that after ~13 hours the J_{sc} it is reduced to $\leq 25\%$ of its peak value. After this period all devices exhibit an increase in series resistance, which is evident from the decrease in the gradient of the J - V characteristic where it crosses the voltage axis: **Figure 2** (a). In most cases this manifests as a deterioration in FF (as shown in Figure 1), although in some cases this is offset by an increase in shunt resistance (e.g. Figure S6).

It is evident from the photographs of devices with a BCP|Ag cathode before and after stability testing (Figure 2 (b) and (c)) that the perovskite layer that is not underneath the Ag electrode has decomposed, since the deep brown colour typical of the perovskite has reverted to a pale yellow/brown colour. Lanzetta *et al.* have shown that organo-tin halide perovskites decompose to form SnI_4 , FAI, GAI and SnO_2 in the presence of O_2 .^[41] Then, SnI_4 reacts with FAI to produce the double perovskite FA_2SnI_6 which has a greatly reduced absorption

coefficient as compared to FASnI_6 .^[42] It is therefore reasonable to expect that the same transition has occurred in those areas not covered by the Ag electrode because O_2 is known to diffuse through C_{60} films^[43] and the BCP layer is so thin (6 nm) that it is almost certainly permeable to gases present in ambient air. It is evident from the photograph of the degraded devices, Figure 2(c), that the metallic silver colour of the metal electrode is only evident on some devices and only in the middle of the electrode, with the rest having reverted to a brown colour. Cross-sectional and top-down SEM imaging; Figure 2 (d) and (e) (Figure S7 and S8) of the degraded area of the Ag electrode shows that the Ag electrode has a lumpy discontinuous appearance indicative of severe degradation. The fact that this degradation is most pronounced at the edges of the electrode is consistent with a process in which corrosive gas emanating from the decomposed perovskite adjacent to the area protected by the Ag electrode plays a large role in degrading the electrode.

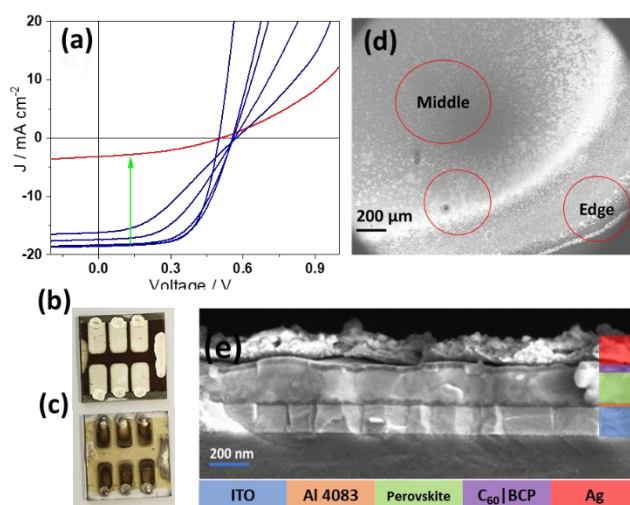


Figure 2| (a) Evolution of the J - V characteristic for an unencapsulated PV device with the structure ITO|PEDOT:PSS (Al 4083)|perovskite| C_{60} |BCP|Ag tested under continuous 1 sun simulated solar illumination in ambient air with the device under at (or very close to) the maximum-power-point.; (b) Photograph of a freshly fabricated device; (c) Photograph of a device after testing in ambient air for 14 hours; (d) SEM image of the Ag electrode of a device

tested in air for 14 hours; (e) Cross-sectional SEM image of a device after testing in air for 14 hours.

To investigate the extent to which corrosive gas emanating from the decomposing perovskite not covered by the Ag electrode contributes to degradation of the electrode, the following experiment was performed: The top three layers of the device stack; C_{60} |BCP|Ag, were deposited onto a glass substrate with the Ag electrodes deposited in strips as shown in **Figure 3** (a). Adjacent to this substrate was placed a *separate* substrate comprising glass perovskite with a C_{60} overlayer and both substrates were subject to 1 sun constant illumination in air for 20 hours. After this period the perovskite film had decomposed and the Ag electrode nearest the perovskite coated substrate was visibly corroded (strip 1). The electrical resistance of the strip electrode nearest the perovskite had increased by $\sim 300\%$, whilst those further away increased by $\sim 30\%$, which is consistent with the hypothesis that gas emanating from the perovskite not protected by the electrode reacts with the electrode to form the insulator AgI. Cross-sectional transmission electron microscopy (TEM) imaging (Figure 3 (b)) with spatially resolved elemental analysis (EDX) (Figure 3 (c) & (d)) of the most visibly corroded edge of Ag strip 1 shows that iodine is present wherever there is Ag, which confirms that iodine containing gas emanates from the perovskite film when it decomposes and is a major contributor to electrode degradation.

Given that SnI_4 is known to decompose to I_2 in the presence of water vapour in air^[41], and that I_2 readily diffuses through C_{60} ^[44] it is reasonable to conclude that the 32.5 nm thick C_{60} layer covering the perovskite is not sufficient to block the ingress of H_2O and so I_2 gas is evolved from the decomposing perovskite. This conclusion is corroborated by the decrease in absorption intensity of the bilayer film within minutes of illumination in air: Figure S9. It is known that Ag reacts spontaneously with I_2 gas to form AgI ^[12] (heat of formation AgI -61.84 kJ / mol) which is a transparent insulator. The conversion of the Ag electrode to AgI explains

why device series resistance increases so quickly, and why the brown colour of the perovskite underneath the Ag electrode becomes visible through the edges of the electrode where conversion of Ag to AgI is most extensive.

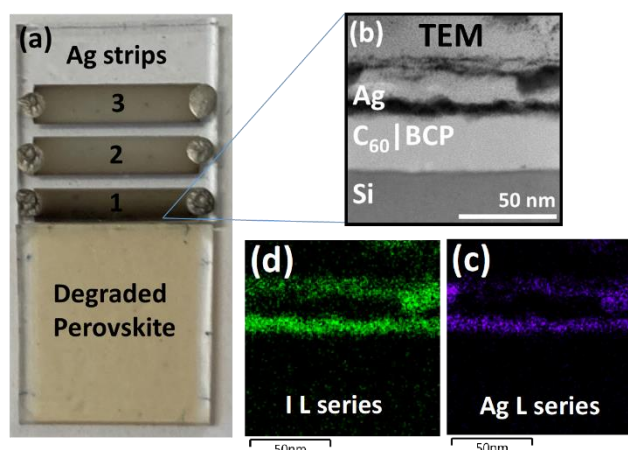


Figure 3 | (a) Photographs showing the experimental set-up used for monitoring the corrosion of Ag electrode by gas emanating from the decomposing perovskite not covered by the electrode. Upper: C₆₀ (32.5 nm) | BCP (6 nm) | Ag (100 nm) strip electrodes; lower perovskite | C₆₀ (32.5 nm) (b) Cross-sectional TEM image of the most degraded part of strip 1; (c) and (d) corresponding EDX analysis elemental maps for I and Ag.

When the Ag electrode is peeled off the degraded device and the BCP and C₆₀ layers are washed away using toluene, SEM imaging shows that the surface morphology of the perovskite film is severely degraded: Figure S10. Elemental analysis using energy dispersive X-ray analysis (EDX) of the perovskite film before and after degradation shows that the Sn:I ratio has reduced from $1:1.15 \pm 0.03$ to $1:0.59 \pm 0.18$, which shows that the perovskite has degraded with the loss of I₂ gas. Notably, the Sn:I ratio for the film before perovskite degradation is much lower than would be expected based on the film composition (approximately 1:2.8) because the film is supported on an indium-tin oxide (ITO) coated glass

substrate and so the Sn signal from the underlying ITO contributes to the Sn signal intensity. The Ag electrode is therefore corroded by I_2 emanating from the underlying perovskite as well as by I_2 from the decomposing perovskite adjacent to the device not covered by the Ag electrode. This result indicates that O_2 and water are able to permeate through the 100 nm Ag electrode and/or that the perovskite has decomposed due to other stressors such as light/heat. However, there is no significant evolution of the electronic absorption spectrum of the tin halide perovskite used in this study when subjected to constant 1 sun illumination in a nitrogen filled glovebox; Figure S11, consistent with the report of Jokar *et al.*^[38] Consequently, light/heat induced degradation of the perovskite over the period of the experiment can be ruled out. This leads us to conclude that diffusion of O_2 and water (present in ambient air) and I_2 gas (formed as a result of degradation of the perovskite not protected by the electrode) through the polycrystalline Ag electrode is the reason for degradation of the perovskite beneath the Ag electrode. Iodine gas is known to catalyse the degradation of tin halide perovskite^[41] and so even a small amount of iodine ingress through the Ag electrode along boundaries between crystallite could give rise to a substantial degradation of the underlying perovskite.

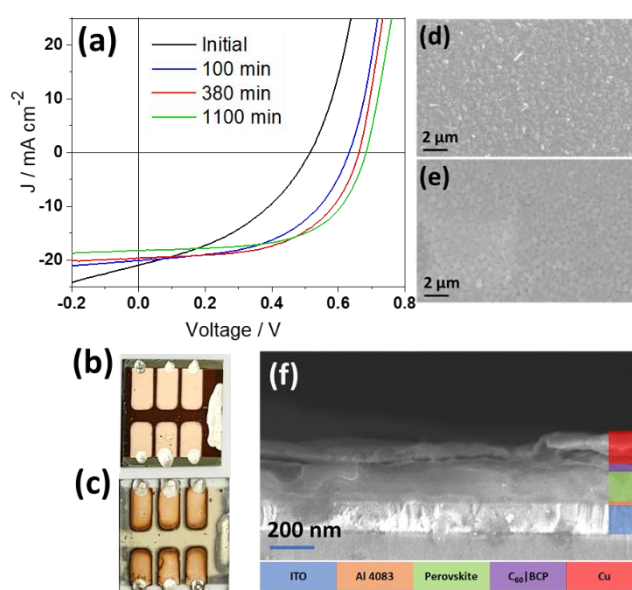


Figure 4 | (a) Evolution of the J - V characteristic for an unencapsulated PV device with the structure ITO|PEDOT:PSS (Al 4083)|perovskite|C₆₀|BCP|Cu tested under continuous 1 sun simulated solar illumination in ambient air with the device under load air for 18.3 hrs.; (b) Photograph of a freshly fabricated device; (c) Photograph of a device after testing in ambient air for 18.3 hours; (d) SEM image of the fresh perovskite; (e) SEM image of the perovskite underneath the Cu electrode in a degraded device after removal of the electrode and organic semiconductor layers; (f) Cross-sectional SEM image of a device after testing in air for 14 hours.

PV devices using a BCP|Cu electrode tested in air typically exhibit a large improvement in V_{OC} , FF , J_{SC} and η within the first few hundred minutes of testing, before stabilising: Figure 1, **Figure 4** (a), Figure S1 and S2. It is evident from the photographs in Figure 4 (b) and (c) of PV devices with a BCP|Cu cathode before and after 18 hours testing that the perovskite not covered by the Cu electrode has decomposed, but the electrodes have retained their characteristic Cu colour over most of their area. When the Cu electrode is peeled off a degraded device and the BCP and C₆₀ layers are washed away using toluene, SEM images reveal that the morphology of the underlying perovskite appears undegraded; Figure 4(d) and (e). EDX elemental analysis confirms this conclusion since the Sn:I ratio is the same, within error, as that of a pristine film: Sn:I $1:19 \pm 0.01$ vs. $1:1.15 \pm 0.03$. This finding is consistent with the cross-sectional SEM analysis of a complete device; Figure 4(f), which shows that the Cu electrode is still of uniform thickness and has not disintegrated after 18 hours constant illumination testing, and the fact that the devices exhibit very little deterioration in FF and V_{OC} and J_{SC} over this period (Figure 4(a) and S2). The small deterioration in J_{SC} can be rationalised in terms of the erosion of the active area from the edges of the electrode, where the electrode has reverted to a deep brown colour indicative of the exposed perovskite. This result supports our earlier

conclusion that degradation of devices using a Ag cathode is due to O₂ and H₂O through the top Ag electrode.

The same experiment as described previously to determine the extent of Ag electrode degradation by I₂ gas emanating from the perovskite not covered by the Ag electrode was performed for devices using Cu electrodes. After 20 hours of 1 sun constant illumination the perovskite has decomposed and the Cu electrode nearest the perovskite coated slide is visibly corroded: **Figure 5** (a). However, in sharp contrast to the case for Ag, the resistance of the Cu electrode that is immediately adjacent to the degraded perovskite *decreased* by $5.1 \pm 2.9\%$ and the strips further away show an even larger decrease in resistance of $13.8 \pm 4.5\%$. Cu is known to react with iodine gas at room temperature to form CuI (heat of formation of CuI -439 kJ / mol) which is transparent semiconductor, and so the smaller reduction in resistance for the electrode nearest the perovskite is consistent with partial conversion of the Cu electrode to CuI. Cross-sectional TEM imaging (Figure 5 (b)) with corresponding EDX analysis (Figure 5 (c), (d) & (e)) of the most corroded edge of strip 1 shows that, in contrast to the case of Ag, the top electrode is still a slab-like film and iodine has not permeated all the way through the Cu electrode. Collectively these data show that a Cu electrode of the same thickness as a Ag electrode is far more resistant to reaction with I₂ gas.

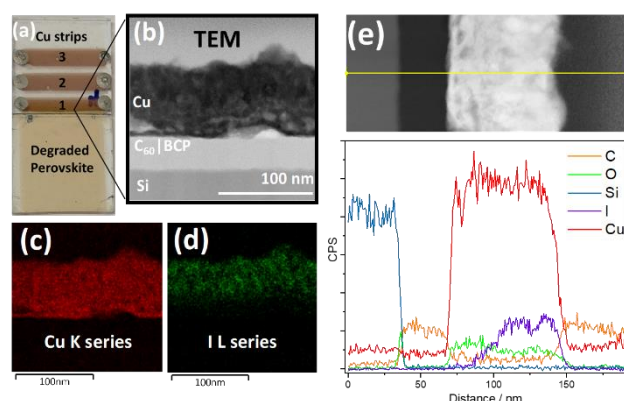


Figure 5(a) Photograph of the experimental set-up used for monitoring the resistance change of Cu electrodes exposed to I₂ gas emanating from decomposing perovskite; (b) Cross-sectional TEM image of the degraded Cu strip; (c) and (d) EDX elemental maps for Cu and I respectively;

(e) EDX line profiles from the cross-section of the degraded Cu strip. Notably, (i) oxygen is present throughout the Cu film cross-section because the sample was briefly exposed to ambient air when transferring to the TEM.; (ii) the thickness of the Cu electrode at the edge of the Cu strip electrode is less than 100 nm due to mask shadowing during Cu evaporation.

To determine why Cu electrodes should be more stable towards corrosion by I₂ gas than Ag, and why the resistance of the Cu electrode decreases upon illumination (even when the top surface has reacted with I₂) the effect of prolonged constant illumination on the morphology of the top electrode was studied: 100 nm thick Cu and Ag electrodes with the same width as used in PV devices were evaporated onto glass|C₆₀ (32.5 nm)|BCP (6 nm) and subject to constant 1 sun illumination for 20 hours in ambient air. Over this period the resistance of 100 nm Ag film strips increased by $43 \pm 16 \%$, an increase that correlates with an increase in surface roughness, measured using an atomic force and scanning electrode microscopy (AFM and SEM respectively): **Figure 6** (a) and (b) and Figure S12. The root-mean-square roughness of the 100 nm strip Ag measured over an area of $5 \times 5 \mu\text{m}$ increased from $0.85 \pm 0.06 \text{ nm}$ to $1.1 \pm 0.1 \text{ nm}$ due to the formation of circular protrusions with diameters of 50-100 nm and heights of $\sim 10 \text{ nm}$. Over the same time period the roughness of the C₆₀|BCP not covered with metal (Figure S13) decreased, which indicates that the increase in surface roughness of the Ag film is not associated with morphological change of the underlying C₆₀|BCP layers.

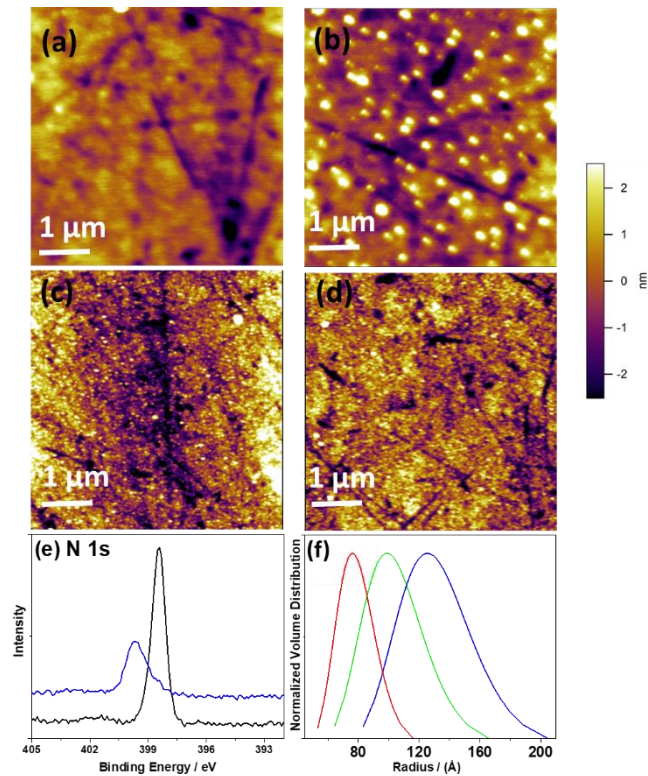


Figure 6 | AFM images of the morphology of (a) glass|C₆₀|BCP|Ag (100 nm) strip; (b) glass|C₆₀|BCP|Ag (100 nm) strip after exposure to constant 1 sun illumination for 20 hours; (c) glass|C₆₀|BCP|Cu (100 nm) strip; (d) glass|C₆₀|BCP|Cu (100 nm) strip after exposure to constant 1 sun illumination for 20 hours. The linear grooves in the AFM images are associated with the underlying glass substrate; (e) HR-XPS analysis of N 1s peak region for BCP (black) and BCP|Cu (blue). The reduction in signal intensity is attributed to partial removal of the BCP when exposing the buried BCP|Cu interface for analysis.; (f) Small angle scattering measurements for Cu and Ag films: (red) Si|C₆₀|BCP|Cu; (green) Si|Cu; (blue) Si|C₆₀|BCP|Ag.

The roughness increase for a 30 nm Ag film was even more pronounced; 780 ± 20 pm to 2.5 ± 0.2 nm (Figure S14 (a) and (b)), which is consistent with the expectation that morphological instability of thin metal films scales inversely with metal film thickness due to the thermodynamic drive for the metal to minimise its surface to volume ratio. Together, the increase in electrical resistance and increase in surface roughness upon illumination indicate that the atoms of the Ag film are highly mobile and tend to aggregate, with the inevitable

consequence that gaps open between the Ag crystallites making up the film. Further evidence that the Ag film is intrinsically fragile is provided by the following experiment: When a 100 nm thick Ag film supported on a C₆₀|BCP bilayer was detached from the substrate by submerging in water followed by washing with toluene (which dissolves the underlying BCP and C₆₀ layers) it disintegrated into small fragments rather than remaining as an intact film: Figure S15 (a). This structural fragility and instability are important in the current context, not only because of the erosion of electrode conductivity, but also because it makes the electrode more transparent to the diffusion of gases through it.

In a stark reversal of the behaviour exhibited for 100 nm Ag films, the resistance of 100 nm Cu strip electrodes *decreased* by 12.9 ± 6.2 % upon constant 1 sun simulated illumination for 20 hours in ambient air. Additionally, AFM images of the strips before and after constant illumination (Figure 6 (c) and (d)) show that the root-mean-surface roughness *decreases* from 1.4 ± 0.12 nm to 1.0 ± 0.08 nm (measured over an area of 5×5 μm). The reduction in sheet resistance can therefore (at least in part) be attributed to the reduction in surface roughness, which reduces losses associated with electron scattering from the Cu film surface. Even when the Cu thickness is reduced to 30 nm there is still a decrease in surface roughness from 630 ± 10 pm to 550 ± 8 pm respectively (Figure S14 (c) and (d)). Furthermore, when a 100 nm thick Cu film supported on a C₆₀|BCP bilayer is floated off in water, followed by washing with toluene to dissolve the underlying BCP and C₆₀ layers, the metal film remains intact: Figure S15 (b). X-ray diffraction shows that both Ag and Cu films are polycrystalline (Figure S16) and so, the stark difference in the robustness of the free standing 100 nm thick Ag and Cu films indicates that the Ag crystallites are less strongly bound to one another than Cu crystallites in the films.

The pronounced difference in the morphological stability of these 100 nm thick Ag and Cu electrodes could result from: **(i)** a difference in the strength of adhesion between the metal

the underlying layer. Previous work by our group and has shown that the morphology, resistivity and stability of optically thin Ag and Cu films towards oxidation in air is strongly dependent on the strength of interaction with the underlying substrate.^[22,45] This is because metal films that bind strongly to the underlying substrate form compact slab-like morphologies at low film thickness that are inherently more resistant to oxidation and morphological change.^[22,45,46] In the current case the resistance of the Cu electrode actually decreases upon constant illumination for 20 hours in ambient air, which evidences the fact that Cu films oxidise extremely slowly in air.; **(ii)** and/or the much lower cohesion energy of Ag atoms as compared to Cu; -249 kJ/mol *vs* -422 kJ/mol respectively in the bulk.^[47] A lower cohesion energy means that metal atoms at the surface of the metal crystallites can move more easily, enabling more facile morphological change at low temperature.; **(iii)** and/or a difference in the rate of surface oxide formation, which is important because morphological change requires diffusion of metal atoms over the crystallite surfaces - a process that is impeded by the formation of an oxide layer. The enthalpy of formation of Ag₂O and Cu₂O is -30.6 kJ/mol and -166.7 kJ/mol respectively and so both reactions occur spontaneously. However, in practice the rate of oxidation of Ag is extremely slow and Ag₂S is formed instead of Ag₂O.^[48] In contrast, the first nanometre of Cu oxidation occurs quickly, followed by extremely slow growth of a thicker layer when the Cu film is compact and slab-like.^[46] Consequently, the rapid formation of an extremely thin oxide layer at the surface of Cu would be expected to hinder morphological evolution of the underlying metal by hindering Cu atom diffusion at the surface.

Given that the strength of the interaction between the incoming Cu atoms and the receiving substrate is an important determinant of the compactness of Cu films^[45], X-ray photoelectron spectroscopy (XPS) (Figure 6 (e) and Figure S17) was used to probe the nature of interaction between Cu and BCP. For this study a 100 nm thick Cu film was evaporated onto a 6 nm thick BCP film supported on a glass substrate. The Cu film was then peeled off to reveal

the buried BCP | Cu interface. Figure 6(e) shows that there is a large increase in the N 1s binding energy upon Cu deposition, which is indicative of a strong interaction between Cu and the N atoms in the bay area of the phenanthroline ring, similar to that reported to occur between evaporated Ag and BCP^[49]. Small angle X-ray scattering measurements (Figure 6 (f)) show that the mean crystallite radius for Cu deposited on BCP is 7.9 ± 0.2 nm which is ~40% smaller than that of Ag, 13.3 ± 0.2 nm, consistent with a higher density of nucleation sites for Cu than Ag and/or a lower mobility of Cu atoms over the BCP surface during film growth. Both possibilities are consistent with a stronger interaction between Cu and BCP than between Ag and BCP. When a Cu film of the same thickness is deposited onto a silicon wafer with native surface oxide - a substrate onto which Cu atoms are known to interact weakly - the mean crystallite size and distribution of sizes is a factor of 35% larger than on BCP, which is further evidence that the binding interaction between BCP molecules and the incoming Cu atoms helps to immobilise Cu atoms when they condense on the BCP film surface. The important role played by BCP in seeding the formation of a compact Cu film is provided by the stability data when the BCP layer is removed: PV devices tested in air are very stable, with the η dropping by only 2-14% over 17.3 hours (Figure 1). At first glance, this is consistent with reports that Cu interacts strongly with C₆₀ due to a ground state charge transfer reaction: See for example reference 44. However, when tested in a nitrogen atmosphere the same devices do not exhibit the same degree of stability as those with a BCP interlayer; Figure S18, with a significant proportion exhibiting a marked deterioration in FF . This indicates that BCP plays an important role in helping to stabilise the C₆₀|Cu interface under inert conditions, and is consistent with a report by Katz *et al.* that Cu diffuses into C₆₀ films - a process that would ultimately be expected to decrease PV device shunt resistance and FF . It has also been reported that O₂ diffuses through C₆₀ films and forms CuC₆₀O_x at the buried interface between C₆₀ and Cu.^[44] It is therefore plausible that the formation of this ternary compound is sufficient to stabilise the C₆₀|Cu interface in air. Notably, devices using a Ag electrode without a BCP charge extraction layer all short-circuit,

which is attributed to rapid diffusion of Ag through the C₆₀ layer forming filamentary shunts, since Firlej *et al.* have reported evidence for rapid Ag electrode diffusion into C₆₀ films and shown it to be electric field induced.^[50]

Conclusions

In summary, we have shown that a thermally evaporated Cu | bathocuproine reflective top electrode is remarkably effective at stabilising unencapsulated inverted organo-tin halide perovskite PV devices towards degradation in ambient air when tested under continuous 1 sun simulated solar illumination under electrical load. The bathocuproine layer is shown to play an important role in nucleating a compact slab-like Cu film, a morphology that is needed to retard oxidation of the electrode in ambient air and adverse reaction with I₂ gas, as well as blocking the ingress of oxygen and water molecules through the top electrode into the device. More generally, the findings of these experiments show that Cu should be the metal of choice for the reflective cathode in inverted tin perovskite PVs when the material interfacing the Cu (in this case BCP) interacts strongly with it, enabling compact Cu film formation and a stable interface towards Cu diffusion into the adjacent charge transport layer. We also envisage that, far from being a disadvantage, the higher susceptibility of Cu toward oxidation in air than Ag or Au could be an advantage in fully encapsulated devices because the rate of oxidation of compact slab-like copper films is actually very slow after the few nanometres. Consequently, a Cu electrode in a fully encapsulated PV device could serve the dual purpose of low-cost reflective electrode and built-in desiccant for oxygen and water ingress, helping to further extend device lifetime.

Experimental Methods

Substrate cleaning

Substrates were cleaned by ultrasonic agitation in a dilute solution of surfactant followed by deionized water, acetone and isopropyl alcohol (IPA) for 15 minutes each. They were then dried using a stream of nitrogen and were UV-O₃ treated for 15 minutes immediately before use.

Device fabrication

PEDOT:PSS (Al 4083) was deposited onto freshly UV-O₃ treated ITO by dropping onto the ITO so as to cover the entire substrate, then spinning at 5000 rpm for 60 seconds in ambient air followed by a 10 minutes annealing at 120°C. Then these electrodes were transferred to a nitrogen-filled glovebox (≤ 1 ppm O₂ and H₂O) for the rest of device fabrication. FA_{0.78}GA_{0.2}SnI₃-1% EDAI₂ + 10 mol % SnF₂ from DMSO was spin coated at 5000 rpm for 90 seconds. Chlorobenzene (600 μ L) was dropped onto the still wet perovskite film 35 seconds after the start of spin coating. The resulting perovskite film was annealed at 70°C for 15 minutes to drive off residual DMSO. The film was then transferred to a vacuum evaporator co-located in the same glovebox and a 32.5 nm layer of C₆₀ was deposited by thermal evaporation at a rate of 0.1-0.4 \AA s^{-1} . The device was completed by evaporating a 5 nm BCP layer at a rate of 0.6-0.7 \AA s^{-1} followed by 100 nm of Ag or Cu at 1-1.5 \AA s^{-1} . Thermal evaporations were performed at a pressure of 2×10^{-6} mbar with substrate rotation. The Ag or Cu electrode was deposited through a shadow mask to make six devices per slide, each with an area of 6 mm². Devices fabricated using a Ag electrode without a BCP layer all short-circuited and so are not included in this study.

Device testing

Device testing was performed in the same nitrogen filled glove box as used for device fabrication (≤ 1 ppm O₂ and H₂O) using an ABET Technologies Sun 2000 solar simulator. Current density–voltage (*J-V*) curves were measured using a Keithley 2400 source-meter under

AM1.5 G solar illumination at 100 mW cm^{-2} (1 sun), scanned from -0.2 V to $+1 \text{ V}$ at 0.1 Vs^{-1} . J - V measurements were made using custom LabVIEW program. Stability tests were performed under continuous 1 sun simulated solar illumination (Xenon short arc lamp, AM1.5 G solar illumination at 100 mW cm^{-2}) with the device under load at a fixed voltage bias close to the maximum-power-point. During device testing the temperature of the device increases to $\sim 43^\circ\text{C}$.

Electrode stability studies

Substrates were prepared by evaporating $2 \text{ mm} \times 12 \text{ mm}$ strips of 100 nm of Cu (or Ag) supported on to C_{60} (32.5 nm) and BCP (5 nm) on a glass substrate. All the electrodes were subjected to continuous 1 sun simulated solar illumination in ambient air and the resistance was measured at regular intervals. The number of samples of each type was four and the resistance was measured using the 2-point probe method. Electrical contact was made using two parallel strips of Ag along the full length of rectangular samples. The distance between the parallel silver electrodes was measured using a caliper.

Electronic absorption spectroscopy

Far-field transmittance of metal films on glass were measured over the wavelength range of $350\text{-}850 \text{ nm}$ using 150 mm . Spectral on Integrating Sphere coupled to PerkinElmer LAMBDA high performance series of UV/vis spectrometer. The incident beam passed through the substrate first.

Scanning transmission electron microscopy (STEM)

Cross-sectional TEM specimens were prepared using a focused ion beam. The specimens were observed and analysed in a double aberration corrected JEOL ARM 200F TEM, equipped with a 100 mm^2 Oxford Instruments windowless EDX detector.

X-ray photoelectron spectroscopy (XPS)

XPS analysis was performed using a Kratos AXIS Ultra DLD spectrometer. In an inert environment the samples were peeled onto a carbon tape and transferred from the glovebox to the spectrometer using an inert atmosphere transfer arm. XPS measurements were carried out in

an ultrahigh vacuum system with a base pressure of 5×10^{-11} mbar. The sample was excited with X-rays from a monochromated Al K α source ($h\nu = 1,486.7$ eV), with the photoelectrons being detected at a 90° take-off angle. Curve fitting was performed using the Casa XPS package, incorporating Voigt (mixed Gaussian Lorentzian) line shapes and a Shirley background.

Atomic force microscopy (AFM)

AFM imaging was performed in tapping mode using an Asylum Research MFP-3D to determine the step height of the films and morphologies.

Scanning electron microscopy (SEM)

SEM imaging was performed using a Zeiss SUPRA 55VP field emission gun SEM. EDXS spectra were recorded using an Oxford Instruments Si-Li detector unit on the SEM instrument, at an accelerating voltage of 20 keV. Cross-sectional SEM images were obtained using a Zeiss ZEISS Gemini 500 with an accelerating voltage of typically 0.5 keV.

GISAXS

Grazing incidence small-angle X-ray scattering (GISAXS) measurements were made using a Xenocs Xeuss 2.0 equipped with a micro-focus Cu K α source collimated with Scatter less slits and Pilatus 300k detector. (Full details are given in Supporting Information accompanying this paper).

XRD

XRD measurements were made on a 3rd generation Malvern Panalytical Empyrean equipped with multicore (iCore/dCore) optics and a Pixel3D detector operating in 1D receiving slit mode. A Cu tube was used giving Cu K $\alpha_{1/2}$ radiation (1.5419 Å). Grazing incidence measurements with an incidence angle of 0.5° were made in the range 15 – 90° 2 θ with a step size of 0.04° and a counting time of ~ 1.4 s/step.

Supporting Information

All data supporting this study are provided as supplementary information accompanying this paper.

Author Contributions

The manuscript was written through contributions of all authors. All authors have given approval to the final version of the manuscript.

Funding Sources

The authors would like to thank the University of Warwick for the award of a Chancellor's International Scholarship to Anjana Wijesekara.

Received: ((will be filled in by the editorial staff))
Revised: ((will be filled in by the editorial staff))
Published online: ((will be filled in by the editorial staff))

References

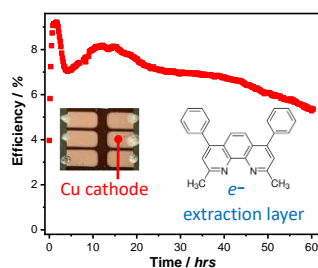
- [1] J. Cao, F. Yan, *Energy Environ. Sci.*, **2021**, *14* (3), 1286.
- [2] L. Xu, X. Feng, W. Jia, W. Lv, A. Mei, Y. Zhou, Q. Zhang, R. Chen, W. Huang, *Energy Environ. Sci.* **2021**, *14*, 4292.
- [3] A. Babayigit, A. Ethirajan, M. Muller, B. Conings, *Nat. Mater.* **2016**, *15*, 247.
- [4] W. Shockley, H. J. Queisser, *J. Appl. Phys.* **1961**, *32*, 510.
- [5] W. Ke, M. G. Kanatzidis, *Nat. Commun.* **2019**, *10*, 965.
- [6] M. Jeevaraj, S. Sudhakar, M. K. Kumar, *Mater. Today Commun.* **2021**, *27*, 102159.
- [7] C. C. Boyd, R. Checharoen, T. Leijtens, M. D. McGehee, *Chem. Rev.* **2019**, *119*, 3418.
- [8] M. Kaltenbrunner, G. Adam, E. D. Głowacki, M. Drack, R. Schwödiauer, L. Leonat, D. H. Apaydin, H. Groiss, M. C. Scharber, M. S. White, N. S. Sariciftci, S. Bauer, *Nat.*

- Mater.* **2015**, *14*, 1032.
- [9] W. Chen, Y. Wu, Y. Yue, J. Liu, W. Zhang, X. Yang, H. Chen, E. Bi, I. Ashraful, M. Grätzel, L. Han, *Science* **2015**, *350*, 944.
- [10] Kitco, *Historical London Fix Prices Current Year*, **2021**.
- [11] S. Cacovich, L. Ciná, F. Matteocci, G. Divitini, P. A. Midgley, A. Di Carlo, C. Ducati, *Nanoscale* **2017**, *9*, 4700.
- [12] Y. Kato, L. K. Ono, M. V. Lee, S. Wang, S. R. Raga, Y. Qi, *Adv. Mater. Interfaces* **2015**, *2*, 1500195.
- [13] S. Svanström, T. J. Jacobsson, G. Boschloo, E. M. J. Johansson, H. Rensmo, U. B. Cappel, *ACS Appl. Mater. Interfaces* **2020**, *12*, 7212.
- [14] J. Li, Q. Dong, N. Li, L. Wang, *Adv. Energy Mater.* **2017**, *7*, 1602922.
- [15] M. Jørgensen, K. Norrman, F. C. Krebs, *Sol. Energy Mater. Sol. Cells* **2008**, *92*, 686.
- [16] F. Behrouznejad, S. Shahbazi, N. Taghavinia, H. P. Wu, E. Wei-Guang Diao, *J. Mater. Chem. A* **2016**, *4*, 13488.
- [17] H. J. Pereira, R. A. Hatton, *ACS Appl. Mater. Interfaces* **2019**, *11*, 43.
- [18] J. Zhao, X. Zheng, Y. Deng, T. Li, Y. Shao, A. Gruverman, J. Shield, J. Huang, *Energy Environ. Sci.* **2016**, *9*, 3650.
- [19] F. Fu, S. Pisoni, Q. Jeangros, J. Sastre-Pellicer, M. Kawecki, A. Paracchino, T. Moser, J. Werner, C. Andres, L. Duchêne, P. Fiala, M. Rawlence, S. Nicolay, C. Ballif, A. N. Tiwari, S. Buecheler, *Energy Environ. Sci.* **2019**, *12*, 3074.
- [20] A. K. Chauhan, P. Kumar, *J. Mater. Sci. Mater. Electron.* **2019**, *30*, 9582.
- [21] C. T. Lin, J. Ngiam, B. Xu, Y. H. Chang, T. Du, T. J. Macdonald, J. R. Durrant, M. A. McLachlan, *J. Mater. Chem. A* **2020**, *8*, 8684.
- [22] P. Bellchambers, M. Walker, S. Huband, A. Dirvanauskas, R. A. Hatton, *ChemNanoMat* **2019**, *5*, 619.
- [23] I. Platzman, R. Brenner, H. Haick, R. Tannenbaum, *J. Phys. Chem. C* **2008**, *112*, 1101.

- [24] S. Choudhary, J. V. N. Sarma, S. Pande, S. Ababou-Girard, P. Turban, B. Lepine, S. Gangopadhyay, *AIP Adv.* **2018**, *8*, 055114.
- [25] P. Li, Z. Wu, H. Hu, Y. Zhang, T. Xiao, X. Lu, Z. Ren, G. Li, Z. Wu, J. Hao, H. L. Zhang, Z. Zheng, *ACS Appl. Mater. Interfaces* **2020**, *12*, 26050.
- [26] N. N. Udalova, E. M. Nemygina, E. A. Zharenova, A. S. Tutantsev, A. A. Sudakov, A. Y. Grishko, N. A. Belich, E. A. Goodilin, A. B. Tarasov, *J. Phys. Chem. C* **2020**, *124*, 24601.
- [27] L. Wang, G. R. Li, Q. Zhao, X. P. Gao, *Energy Storage Mater.* **2017**, *7*, 40.
- [28] B. Li, H. Di, B. Chang, R. Yin, L. Fu, Y. N. Zhang, L. Yin, *Adv. Funct. Mater.* **2021**, *31*, 2007447.
- [29] Y. Deng, Q. Dong, C. Bi, Y. Yuan, J. Huang, *Adv. Energy Mater.* **2016**, *6*, 1600372.
- [30] T. Ye, X. Wang, K. Wang, S. Ma, D. Yang, Y. Hou, J. Yoon, K. Wang, S. Priya, *ACS Energy Lett.* **2021**, *6*, 1480.
- [31] T. Wang, Q. Tai, X. Guo, J. Cao, C. K. Liu, N. Wang, D. Shen, Y. Zhu, C. S. Lee, F. Yan, *ACS Energy Lett.* **2020**, *5*, 1741.
- [32] K. P. Marshall, M. Walker, R. I. Walton, R. A. Hatton, *Nat. Energy* **2016**, *1*, 16178.
- [33] T. Bin Song, T. Yokoyama, C. C. Stoumpos, J. Logsdon, D. H. Cao, M. R. Wasielewski, S. Aramaki, M. G. Kanatzidis, *J. Am. Chem. Soc.* **2017**, *139*, 836.
- [34] T. Bin Song, T. Yokoyama, J. Logsdon, M. R. Wasielewski, S. Aramaki, M. G. Kanatzidis, *ACS Appl. Energy Mater.* **2018**, *1*, 4221.
- [35] Q. Tai, X. Guo, G. Tang, P. You, T. W. Ng, D. Shen, J. Cao, C. K. Liu, N. Wang, Y. Zhu, C. S. Lee, F. Yan, *Angew. Chemie - Int. Ed.* **2019**, *58*, 806.
- [36] J. Cao, Q. Tai, P. You, G. Tang, T. Wang, N. Wang, F. Yan, *J. Mater. Chem. A* **2019**, *7*, 26580.
- [37] K. P. Marshall, M. Walker, R. I. Walton, R. A. Hatton, *J. Mater. Chem. A* **2017**, *5*, 21836.

- [38] E. Jokar, C. H. Chien, C. M. Tsai, A. Fathi, E. W. G. Diau, *Adv. Mater.* **2019**, *31*, 1804835. J. A. Christians, P. Schulz, J. S. Tinkham, T. H. Schloemer, S. P. Harvey, B. J. Tremolet De Villers, A. Sellinger, J. J. Berry, J. M. Luther, *Nat. Energy* **2018**, *3*, 68.
- [39] J. A. Christians, P. Schulz, J. S. Tinkham, T. H. Schloemer, S. P. Harvey, B. J. Tremolet De Villers, A. Sellinger, J. J. Berry, J. M. Luther, *Nat. Energy* **2018**, *3*, 68.
- [40] H. Li, R. Yang, C. Wang, Y. Wang, H. Chen, H. Zheng, D. Liu, T. Zhang, F. Wang, P. Gu, J. Wu, Z. D. Chen, P. Zhang, S. Li, *IEEE J. Photovoltaics* **2019**, *9*, 1081.
- [41] L. Lanzetta, T. Webb, N. Zibouche, X. Liang, D. Ding, G. Min, R. J. E. Westbrook, B. Gaggio, T. J. Macdonald, M. S. Islam, S. A. Haque, *Nat. Commun.* **2021**, *12*, 2853.
- [42] L. Ji, T. Zhang, Y. Wang, P. Zhang, D. Liu, Z. Chen, S. Li, *Nanoscale Res. Lett.* **2017**, *12*.
- [43] M. Jaime, M. Nunez Regueiro, *Appl. Phys. A Mater. Sci. Process.* **1995**, *60*, 289.
- [44] E. A. Katz, D. Faiman, S. Shtutina, N. Froumin, M. Polak, A. P. Isakina, K. A. Yagotintsev, M. A. Strzhemechny, Y. M. Strzhemechny, V. V. Zaitsev, S. A. Schwarz, *Phys. B Condens. Matter* **2001**, *304*, 348.
- [45] J. Lee, M. Walker, S. Varagnolo, S. Huband, R. A. Hatton, *ACS Appl. Energy Mater.* **2019**, *2*, 5198.
- [46] P. Bellchambers, J. Lee, S. Varagnolo, H. Amari, M. Walker, R. A. Hatton, *Front. Mater.* **2018**, *5*, 71.
- [47] M. A. Turchanin, P. G. Agraval, *Powder Metall. Met. Ceram.* **2008**, *47*, 26.
- [48] C. Leygraf, I. O. Wallinder, J. Tidblad and T. Graedel, *Atmospheric Corrosion*, John Wiley & Sons, Inc., Hoboken, NJ, USA, **2016**.
- [49] Z. Ying, X. Yang, J. Zheng, Y. Zhu, J. Xiu, W. Chen, C. Shou, J. Sheng, Y. Zeng, B. Yan, H. Pan, J. Ye, Z. He, *J. Mater. Chem. A* **2021**, *9*, 12009.
- [50] L. Firlej, A. Zahab, F. Brocard, N. Kirova, *Synth. Met.* **1997**, *86*, 2331.

Table of content



Organo-tin halide perovskite photovoltaics without encapsulation, tested in ambient air under electrical load exhibit exceptional stability when using a bathocuproine | copper cathode in an inverted device architecture. It is shown that compact copper electrodes are far more resistant to corrosion by iodine gas, towards adverse morphological evolution, and are less permeable to oxygen and water than conventional silver cathodes.

Supporting Information

Enhanced stability of inverted tin perovskite photovoltaics using a copper top electrode

Anjana Wijesekara¹, Marc Walker², Yisong Han², David Walker², Steven Huband² and Ross Hatton^{1}*

¹ Department of Chemistry, University of Warwick, CV4 7AL, Coventry, United Kingdom.

² Department of Physics, University of Warwick, CV4 7AL, Coventry, United Kingdom.

*Corresponding Author. E-mail: Ross.Hatton@warwick.ac.uk

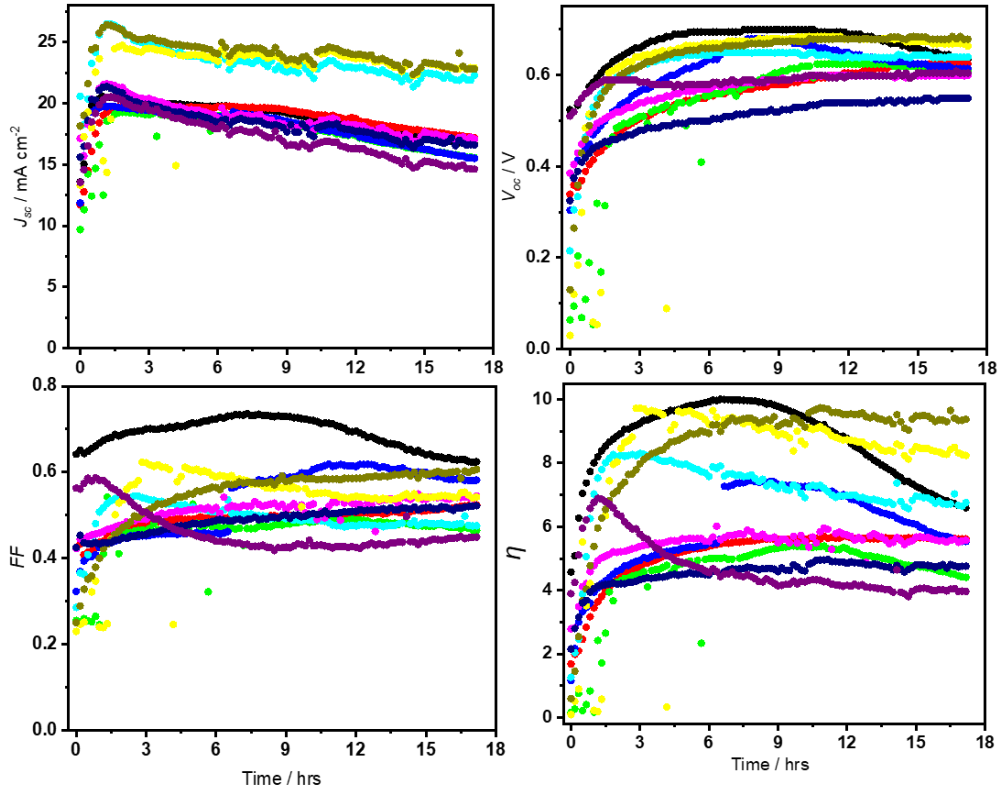


Figure S1| Evolution of the J_{SC} , V_{OC} , FF and η for unencapsulated perovskite PV devices with the architecture ITO|PEDOT:PSS (Al 4083)|perovskite|C₆₀|BCP|Cu tested in ambient air (relative humidity 30-50%) under continuous 1 sun simulated solar illumination with the device under load at (or very close to) maximum-power-point. Perovskite: FA_{0.78}GA_{0.2}SnI₃-1% EDAI₂ with 10 mol % SnF₂.

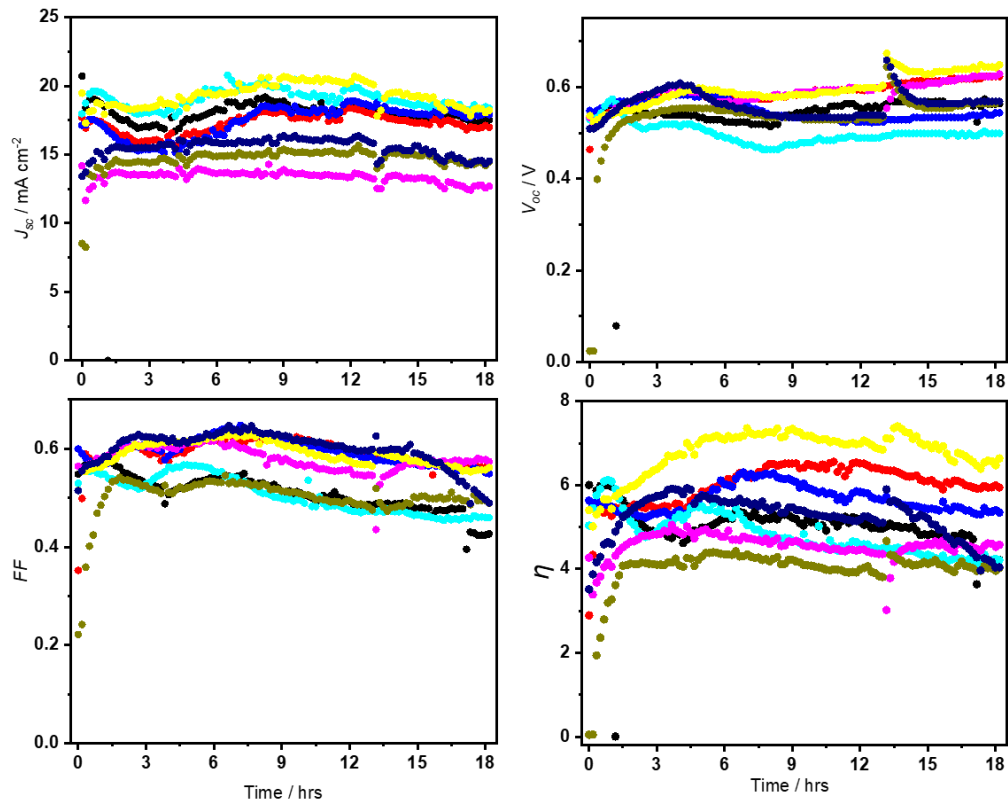


Figure S2 | Evolution of the J_{SC} , V_{OC} , FF and η for unencapsulated perovskite PV devices with the architecture ITO|PEDOT:PSS (Al 4083)|perovskite|C₆₀|Cu tested in ambient air (relative humidity 30-50%) under continuous 1 sun simulated solar illumination with the device under load at (or very close to) maximum-power-point. Perovskite: FA_{0.78}GA_{0.2}SnI₃-1% EDAI₂ with 10 mol % SnF₂.

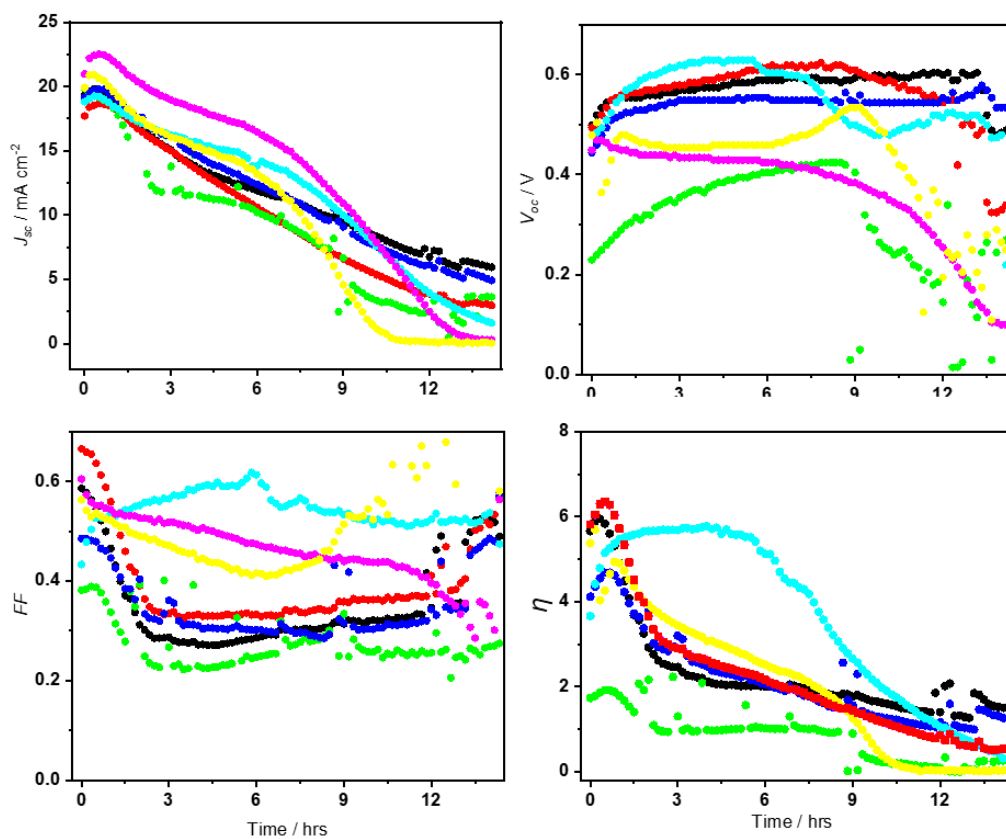


Figure S3 | Evolution of the J_{SC} , V_{OC} , FF and η for unencapsulated perovskite PV devices with the architecture ITO|PEDOT:PSS (Al 4083)|perovskite|C₆₀|BCP|Ag tested in ambient air (relative humidity 30-40%) under continuous 1 sun simulated solar illumination with the device under load at (or very close to) maximum-power-point in air. Perovskite: FA_{0.78}GA_{0.2}SnI₃-1% EDAI₂ with 10 mol % SnF₂.

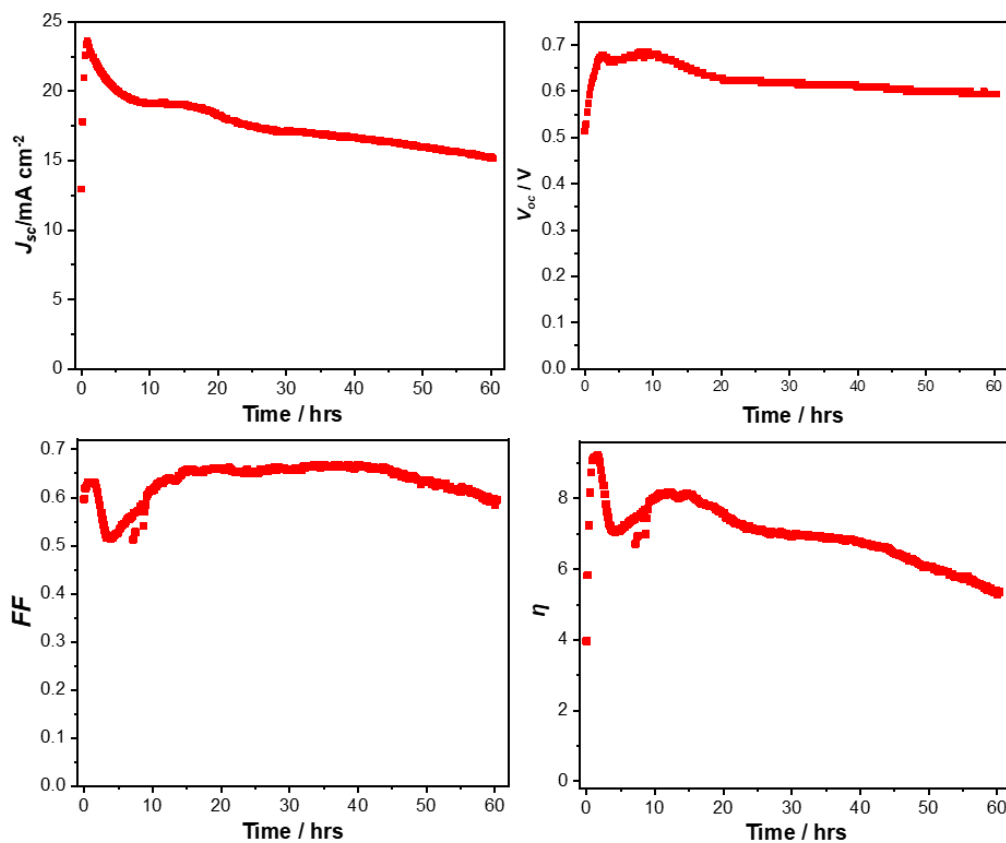


Figure S4 | Evolution of the J_{sc} , V_{oc} , FF and η for a champion unencapsulated perovskite PV device with the architecture ITO|PEDOT:PSS (Al 4083)|perovskite|C₆₀|BCP|Cu tested in ambient air (relative humidity 30-50%) under continuous 1 sun simulated solar illumination with the device under load at (or very close to) maximum-power-point. Perovskite: FA_{0.78}GA_{0.2}SnI₃-1% EDAI₂ with 10 mol % SnF₂.

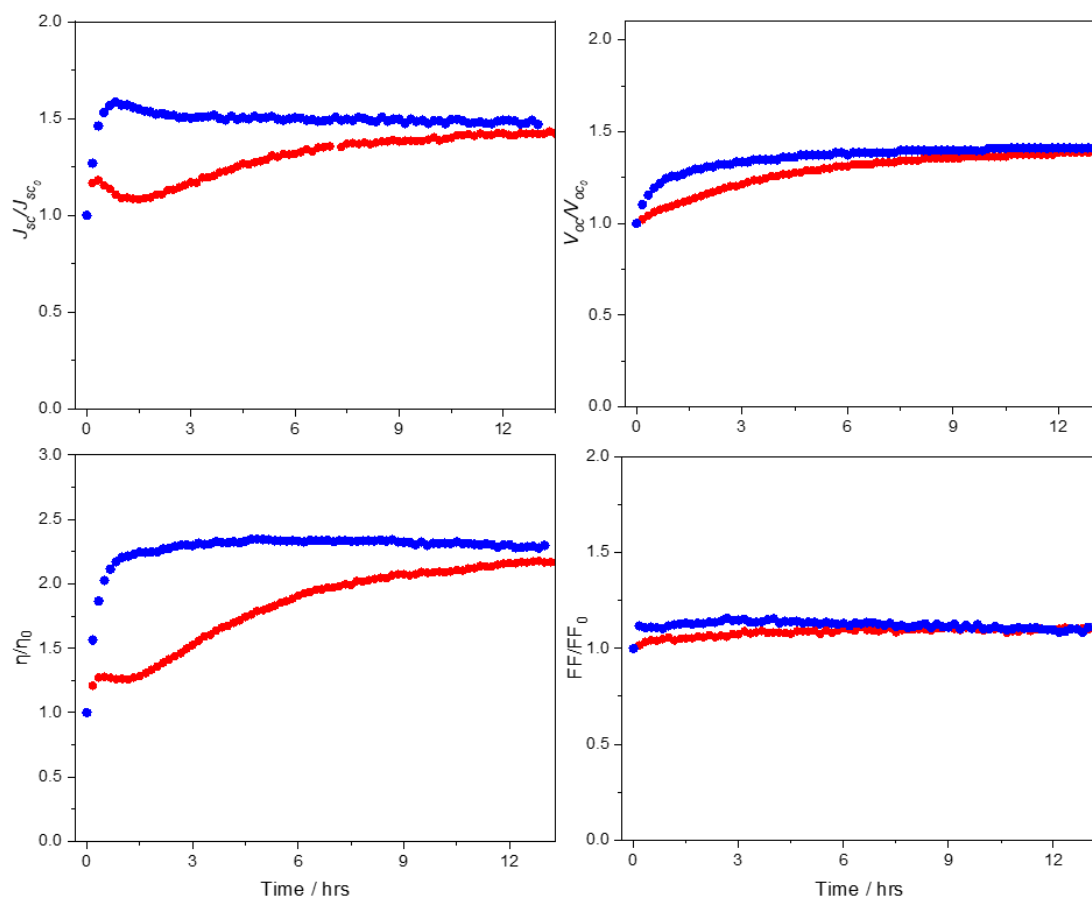


Figure S5 | Evolution of the J_{SC} , V_{OC} , FF and η for unencapsulated perovskite PV devices with the architecture ITO|PEDOT:PSS (Al 4083)|perovskite|C₆₀|Cathode tested in a nitrogen filled glovebox (≤ 1 ppm O₂ and H₂O) under continuous 1 sun simulated solar illumination with the device under load at (or very close to) the maximum-power-point. Perovskite: FA_{0.78}GA_{0.2}SnI₃-1% EDAI₂ with 10 mol % SnF₂. Cathode: (red) BCP|Cu; (blue) BCP|Ag.

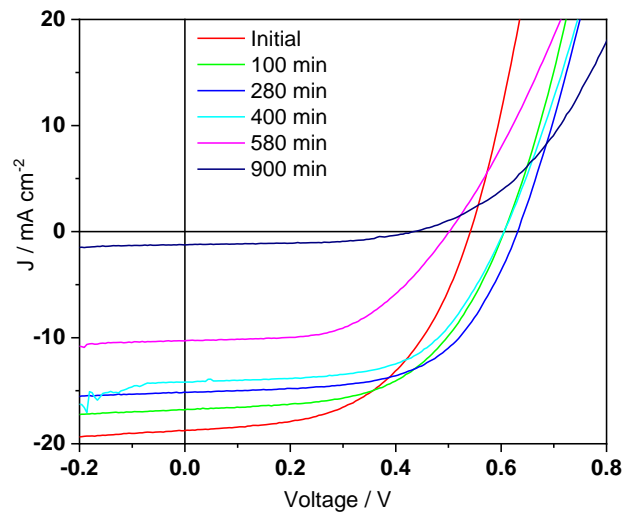


Figure S6 | Evolution of the J - V characteristic for an unencapsulated perovskite PV device with the architecture ITO|PEDOT:PSS (Al 4083)|perovskite|C₆₀|BCP|Ag tested in air under continuous 1 sun simulated solar illumination with the device under load at (or very close to) maximum-power-point. Perovskite: FA_{0.78}GA_{0.2}SnI₃-1% EDAl₂ with 10 mol % SnF₂. In this example the FF is unchanged with device degradation because the increase in series resistance is off-set by an increases in shunt resistance.

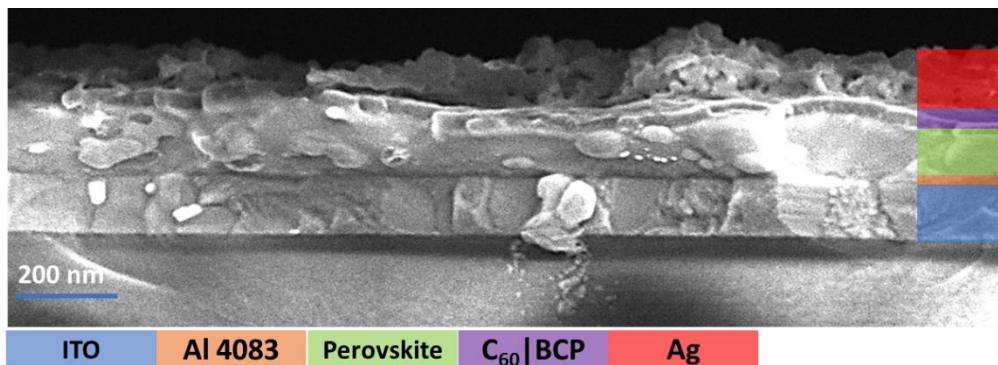


Figure S7 | Cross-sectional SEM image of a PV device with the structure ITO|PEDOT:PSS (Al 4083)|perovskite|C₆₀|BCP|Ag after testing under continuous 1 sun simulated solar illumination in ambient air for 14 hrs with the device at or very close to maximum-power-point.

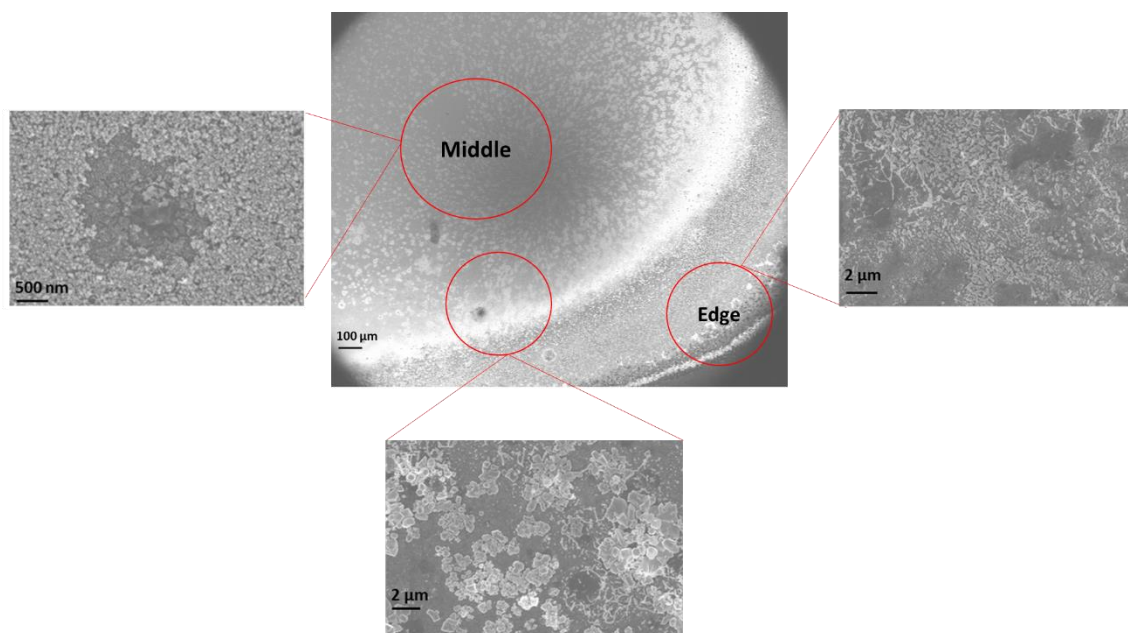


Figure S8 | Representative SEM images of the electrode of a PV device with the structure ITO|PEDOT:PSS (Al 4083)|perovskite|C₆₀|BCP|Ag after testing under continuous 1 sun simulated solar illumination in ambient air for 14 hrs with the device at or very close to maximum-power-point.

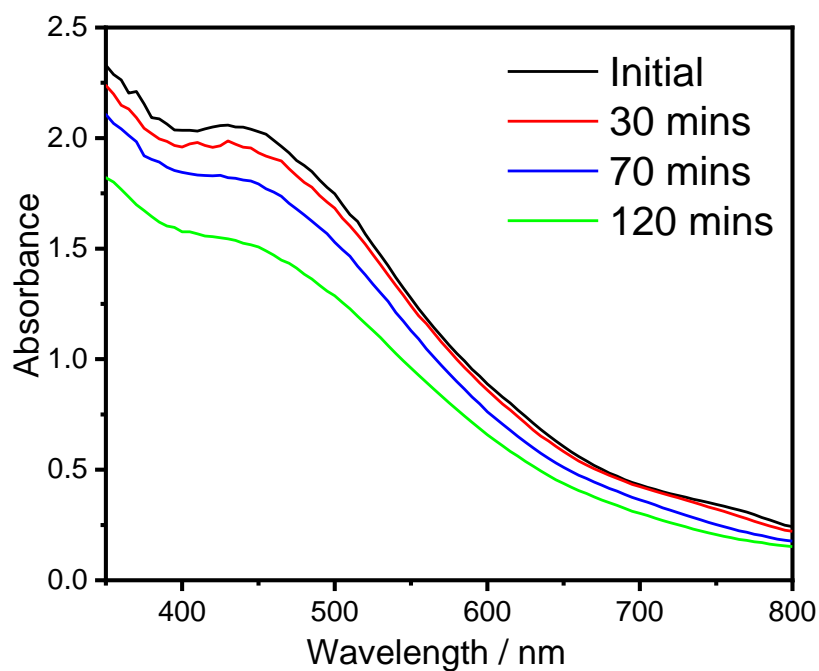


Figure S9 | UV-Visible absorption spectrum of a film of glass|perovskite (100-110 nm)|C₆₀ (32.5 nm) exposed to constant 1 sun simulated illumination in ambient air as a function of time.

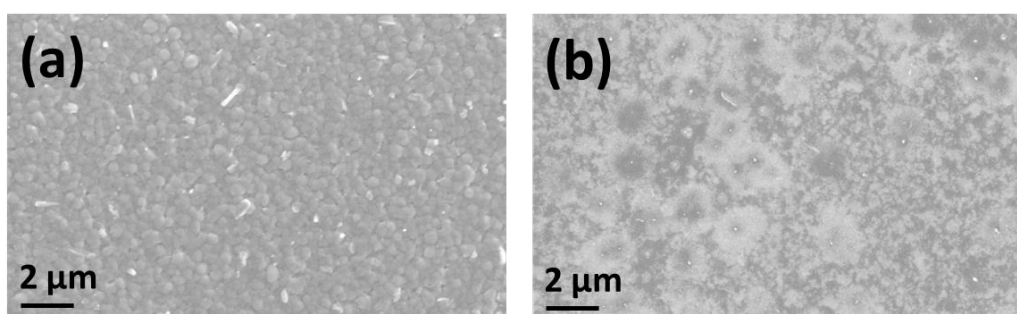


Figure S10 | SEM image of the perovskite as deposited (a) and after device testing in air and removal of the Ag electrode, BCP and C₆₀ layers to expose the perovskite (b).

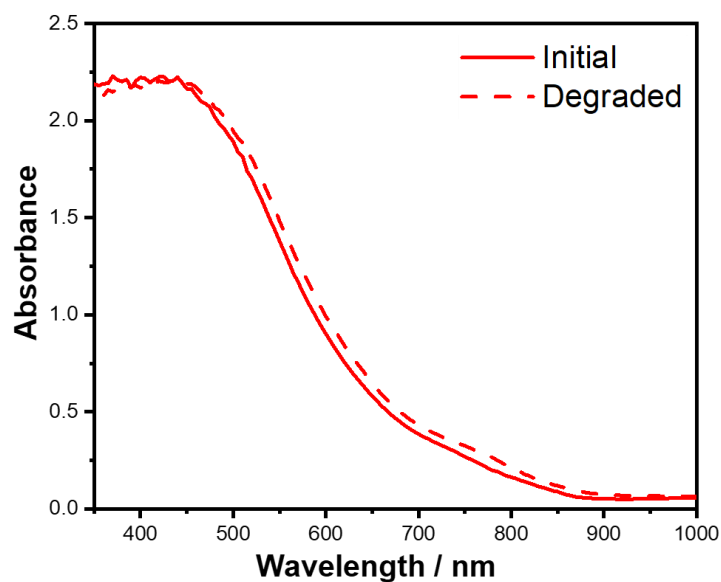


Figure S11 | UV-Visible absorption spectrum of a film of glass|perovskite|C₆₀ exposed to 1 sun simulated solar illumination in a N₂ atmosphere for 14 hours.

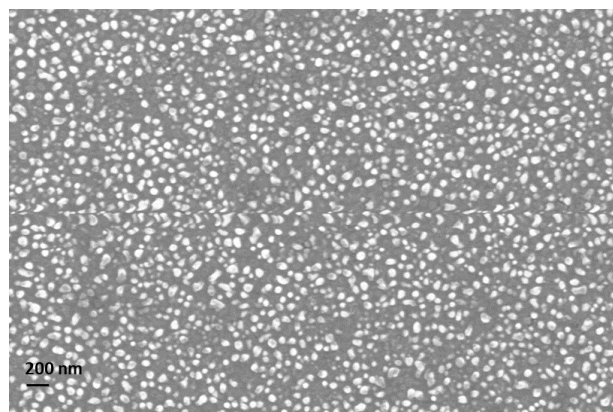


Figure S12| SEM image of glass|C₆₀|BCP|Ag (100 nm) strip after exposure to constant 1 sun illumination for 20 hours in ambient air.

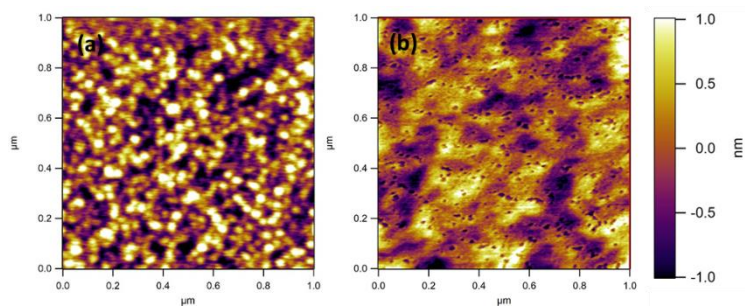


Figure S13| AFM images of the morphology of (a) glass|C₆₀|BCP film; (b) glass|C₆₀|BCP film after exposure to constant illumination for 20 hours in ambient air. The surface roughness measured over an area of $1 \times 1 \mu\text{m}$ is 560 pm and 440 pm respectively.

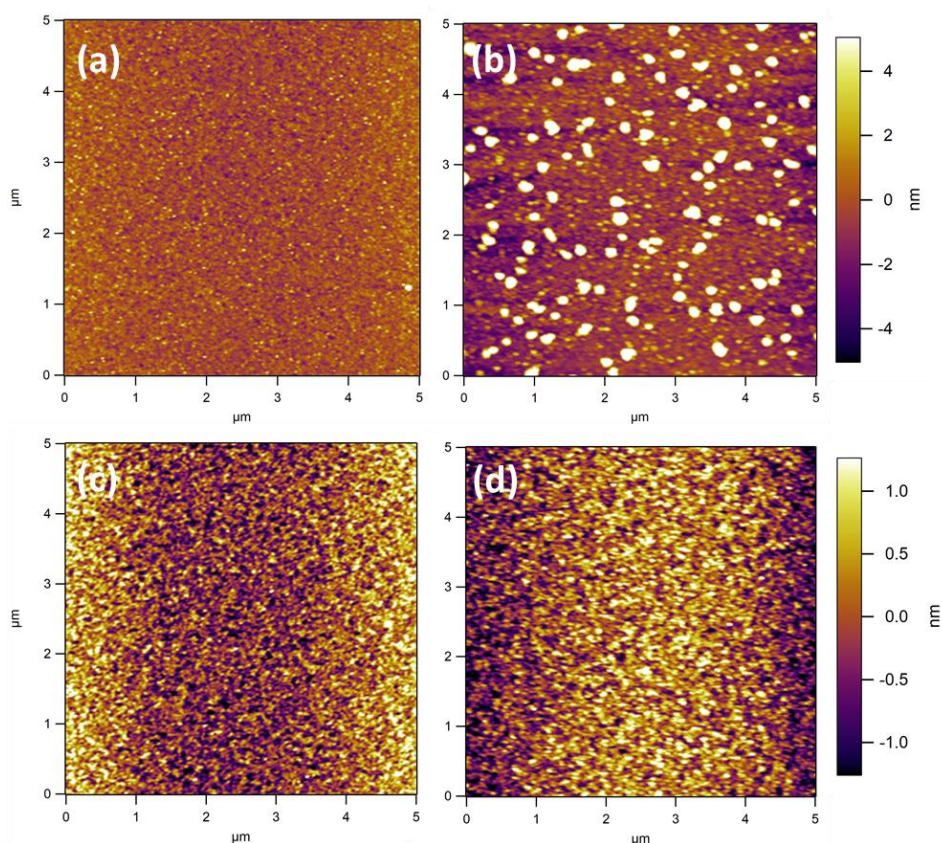


Figure S14 | AFM images of the morphology of **(a)** glass|C₆₀|BCP|Ag (30 nm) film; **(b)** glass|C₆₀|BCP|Ag (30 nm) film after exposure to constant 1 sun simulated solar illumination for 20 hours in ambient air; **(c)** glass|C₆₀|BCP|Cu (30 nm) film; **(d)** glass|C₆₀|BCP|Cu (30 nm) film after exposure to constant 1 sun simulated solar illumination for 20 hours in ambient air.

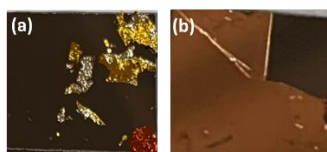


Figure S15 | Photograph of **(a)** 100 nm Ag film supported on silicon|C₆₀|BCP floated off in water and washed with toluene to remove the C₆₀ and BCP layers; **(b)** Photograph of **(a)** 100 nm Cu film supported on silicon|C₆₀|BCP floated off in water and washed with toluene to remove the C₆₀ and BCP layers.

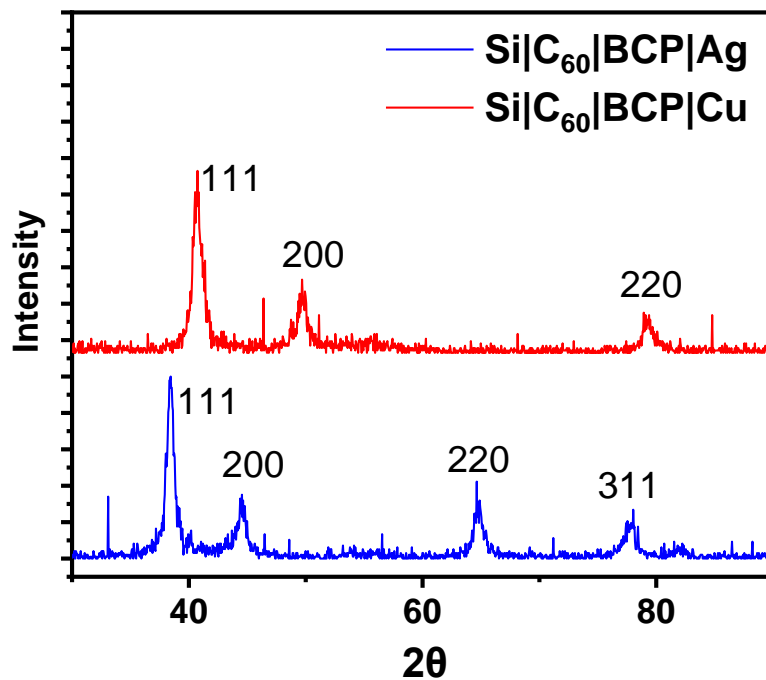


Figure S16 | XRD pattern of 30 nm thick Ag and Cu films supported on Si|C₆₀|BCP. Measurements have been offset vertically along the y-axis for clarity.

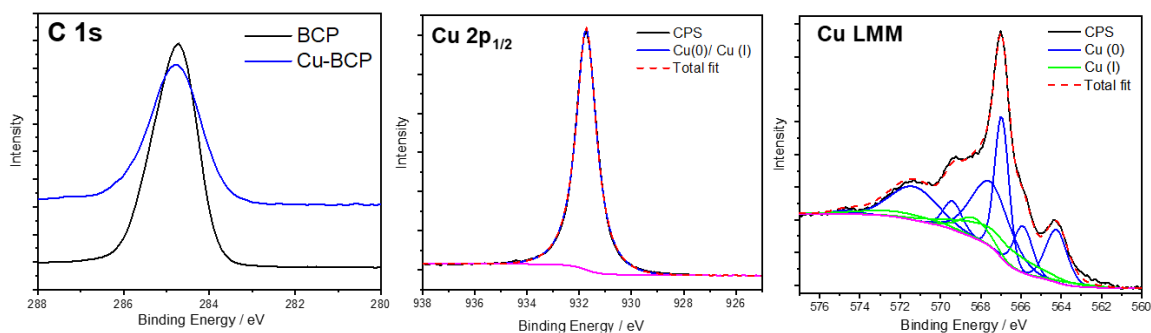


Figure S17 | HR-XPS of C 1s and Cu 2p_{1/2}, and Auger Cu LMM spectral region for BCP and the buried BCP | Cu interface.

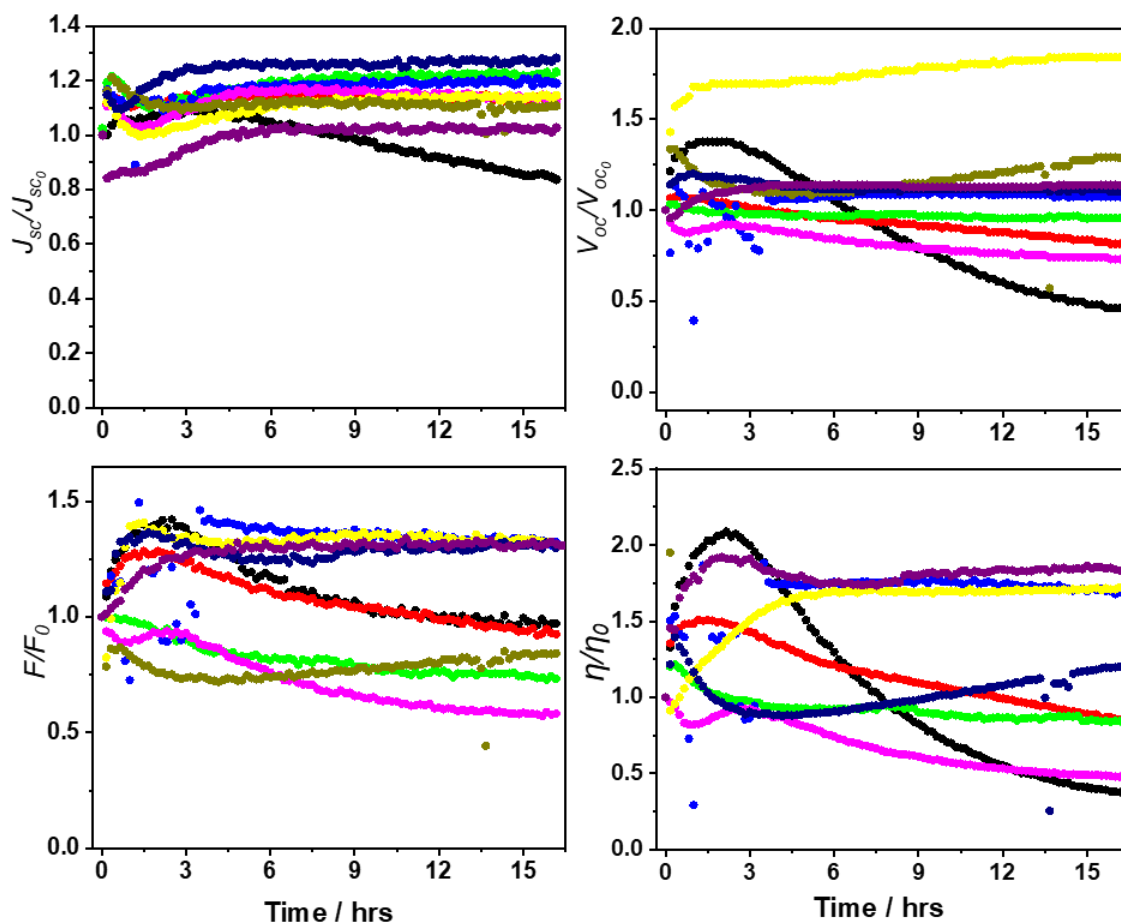


Figure S18 | Evolution of the relative J_{sc} , V_{oc} , FF and η for devices with C_{60}/Cu cathode tested under continuous 1 sun simulated solar illumination with the devices under load at (or very close to) maximum-power-point. Devices were tested in a nitrogen filled glove box (≤ 1 ppm O_2 and H_2O).

Table S1 | Stability of unencapsulated tin halide perovskite PV devices tested in ambient air under 1 sun continuous simulated solar illumination reported in the literature to date.

Perovskite	Conditions RH = Relative Humidity T= Temperature	Time / hrs	Power conversion efficiency retained after test / %	Reference
Inorganic tin perovskite				
CsSnI ₃	RH ~25% Light soaking	22	70%	[1]
CsSnI ₃	RH ~25% Light soaking	20	70%	[2]
CsSnBr ₃	RH 40% Light soaking	5	40%	[3]
CsSnI ₃	RH 40% Light soaking	0.5	40%	[4]
CsSnI ₃	RH ~20% Light soaking	~130	70%	[5]
Organo-tin halide				
FASnI ₃	RH 20% Light soaking	16	50%	[6]
FASnI ₃	RH 20% Light soaking	10	60%	[7]
FASnI ₃	RH 20% Light soaking	2.3	70%	[8]
FA _{0.78} GA _{0.2} SnI ₃	RH 30-50% Under load	17.3 (44.5)	86-100% (70%)	This work (champion)

Experimental Procedures

Grazing incidence small-angle X-ray scattering (GISAXS) measurements were made using a Xenocs Xeuss 2.0 equipped with a micro-focus Cu K α source collimated with Scatterless slits. The scattering was measured using a Pilatus 300k detector with a pixel size of 0.172 mm \times 0.172 mm. The distance between the detector and the sample was calibrated using silver behenate (AgC₂₂H₄₃O₂), giving a value of 2.480(5) m. The magnitude of the scattering vector (q) is given by $q=4\pi \sin(\theta)/\lambda$, where 2θ is the angle between the incident and scattered X-rays

and λ is the wavelength of the incident X-rays. This gave a q range for the detector of 0.003 \AA^{-1} and 0.13 \AA^{-1} in the horizontal plane. This q range allows crystallite sizes between 1 and 200 nm to be determined. Samples were aligned such that the surface was parallel to the beam and in the centre of the beam. To maximize the scattering signal from the Ag or Cu layers the sample was positioned at an incidence angle (α_i) of 0.3° which is close to the critical angle of 0.4° for Ag or Cu with Cu $K\alpha$ radiation. Integrating the in-plane scattering as a function of q allows the horizontal radius of the crystallites to be determined. The horizontal scattering was fitted using spheres with a lognormal distribution of the radius using the Irena analysis package.^[9]

References

- [1] K. P. Marshall, M. Walker, R. I. Walton, R. A. Hatton, *Nat. Energy* **2016**, *1*, 16178.
- [2] K. P. Marshall, M. Walker, R. I. Walton, R. A. Hatton, *J. Mater. Chem. A* **2017**, *5*, 21836.
- [3] T. Bin Song, T. Yokoyama, C. C. Stoumpos, J. Logsdon, D. H. Cao, M. R. Wasielewski, S. Aramaki, M. G. Kanatzidis, *J. Am. Chem. Soc.* **2017**, *139*, 836.
- [4] T. Bin Song, T. Yokoyama, J. Logsdon, M. R. Wasielewski, S. Aramaki, M. G. Kanatzidis, *ACS Appl. Energy Mater.* **2018**, *1*, 4221.
- [5] B. Li, H. Di, B. Chang, R. Yin, L. Fu, Y. N. Zhang, L. Yin, *Adv. Funct. Mater.* **2021**, *31*, 2007447.
- [6] Q. Tai, X. Guo, G. Tang, P. You, T. W. Ng, D. Shen, J. Cao, C. K. Liu, N. Wang, Y. Zhu, C. S. Lee, F. Yan, *Angew. Chemie - Int. Ed.* **2019**, *58*, 806.
- [7] J. Cao, Q. Tai, P. You, G. Tang, T. Wang, N. Wang, F. Yan, *J. Mater. Chem. A* **2019**, *7*, 26580.
- [8] T. Wang, Q. Tai, X. Guo, J. Cao, C. K. Liu, N. Wang, D. Shen, Y. Zhu, C. S. Lee, F. Yan, *ACS Energy Lett.* **2020**, *5*, 1741.

[9] J. Ilavsky, P. R. Jemian, *J. Appl. Crystallogr.* **2009**, *42*, 347.